



Title	Capacitance enhancement by ion-laminated borophene-like layered materials
Author(s)	Kambe, Tetsuya; Katakura, Masahiro; Taya, Hinayo et al.
Citation	Nature Communications. 2025, 16, p. 136
Version Type	VoR
URL	https://hdl.handle.net/11094/100121
rights	This article is licensed under a Creative Commons Attribution-NonCommercial-NoDerivatives 4.0 International License.
Note	

The University of Osaka Institutional Knowledge Archive : OUKA

<https://ir.library.osaka-u.ac.jp/>

The University of Osaka

Capacitance enhancement by ion-laminated borophene-like layered materials

Received: 22 March 2024

Accepted: 5 December 2024

Published online: 27 January 2025

 Check for updates

Tetsuya Kambe  , Masahiro Katakura  , Hinayo Taya², Hirona Nakamura², Takuya Yamashita², Masataka Yoshida², Akiyoshi Kuzume^{4,6}, Kaori Akagami³, Ryota Imai³, Jumpei Kawaguchi³, Shigeyuki Masaoka  , Shoichi Kubo  , Hiroaki Iino  , Atsushi Shishido  & Kimihisa Yamamoto  

Atomically flat two-dimensional networks of boron are attracting attention as post-graphene materials. An introduction of cations between the boron atomic layers can exhibit unique electronic functions that are not achieved by neutral graphene or its derivatives. In the present study, we propose a synthesis strategy for ion-laminated boron layered materials in a solution phase, which enables the preparation of analogs by changing the alkali-metal species. The introduction of large cations extends the thermal range of the liquid-crystal phases because of weakened ionic interactions between borophene-like layers. An investigation of the capacitance of ion-laminated structures revealed a 10⁵-fold or better increase in capacitance when the borophene-like materials were introduced between electrodes. That is difficult for general materials since the dielectric constant of common materials is below several thousand.

Inorganic two-dimensional materials have been widely investigated and used in various electronic devices that play important roles in society. For example, clay minerals or perovskite-structured materials can increase the device capacitances between electrodes. Such materials include BaTiO₃, which exhibits ferroelectricity and high permittivity as a result of shifts of its ions during phase transitions¹⁻³. Recently, layer control of perovskites has also been reported, and their dielectric properties have been elucidated⁴. Because these functions are based on two-dimensionally arranged ions, neutral materials such as graphite or graphene analogs are not suitable for use in the aforementioned applications. In addition, the high physical and chemical stability of inorganic materials is a critical feature that cannot be matched by organic molecular materials and is an important property

for materials used in practical devices. However, the structural rigidity of inorganic materials severely limits their performance and makes them unsuitable for use in high-performance next-generation devices. A rigid structure generally inhibits movement of atoms or molecules under an external stimulus, which might set the upper limit on performance. Because rigidity is a fundamental feature of common inorganic materials, this problem is difficult to overcome.

Single atomic layers of inorganic materials are attracting increasing attention. The preparation of thin films of layered inorganic materials such as MoS₂, WS₂, MoSe₂, MoTe₂, TaSe₂, NbSe₂, NiTe₂, BN, and Bi₂Te₃ has been reported^{5,6}. In addition, monolayer materials composed of only a single element have been studied, with particular emphasis on main-group elements such as silicene^{7,8}, borophene^{9,10},

¹Center for Future Innovation (CFi), Graduate School of Engineering, Osaka University, 2-1 Yamadaoka, Suita, Osaka 565-0871, Japan. ²Laboratory for Chemistry and Life Science, Institute of Integrated Research, Institute of Science Tokyo, Yokohama 226-8501, Japan. ³Division of Applied Chemistry, Graduate School of Engineering, Osaka University, Osaka 565-0871, Japan. ⁴JST-ERATO, Institute of Science Tokyo, Yokohama 226-8501, Japan. ⁵Innovative Catalysis Science Division, Institute for Open and Transdisciplinary Research Initiatives (ICS-OTRI), Osaka University, Suita, Osaka 565-0871, Japan. ⁶Clean Energy Research Center, University of Yamanashi, Kofu 400-8510, Japan. ⁷Laboratory for Future Interdisciplinary Research of Science and Technology, Institute of Integrated Research, Institute of Science Tokyo, Yokohama 226-8501, Japan. ⁸Research Center for Autonomous Systems Materialogy, Institute of Integrated Research, Institute of Science Tokyo, Yokohama 226-8501, Japan.  e-mail: kambe.t.aa@chem.eng.osaka-u.ac.jp; yamamoto@res.titech.ac.jp

and other materials referred to as “Xenes”^{11–15}. Although Xenes have been intensively investigated as Dirac electron systems, the low stability causes various problems to be used as functional materials. In particular, borophene, which has a boron network, has been theoretically proposed as a highly flexible material¹⁶; however, immediate oxidation of borophene in air is a serious problem¹⁰. Recently, bilayer borophenes have been focused to overcome the low stability^{17–19}, however, a single layered borophene requires a metal surface for its existence. In addition, borophane, which is composed of B-H and B-H-B bonds, are also arising as a hydrogenating material. They are synthesized by hydrogenated reaction from borophene²⁰. Focusing on the preparation methods, chemical bottom-up synthesis for the single atomic layers is attractive. Nishihara et al. have reported the design and synthesis of graphene-like inorganic materials with interfacial reactions, where the building blocks are two-dimensional metal complexes with organic ligands^{21,22}.

A material composed of borophene oxide layers, which are graphene-like atomic sheets composed of only inorganic elements, was reported by our research group as alternating layers of single anionic borophene analogs and potassium cations^{23,24}. The borophene oxide layers are chemically synthesized from molecular potassium borohydride. The introduction of metal cations between layers is significant for this material since it enables the formation of a thin film. Metal borides, including MgB_2 , are similar to this material; however, the two-dimensional sheet is difficult without chemical bonding formations such as B-H bondings²⁵. Therefore, these properties are totally different. Such metal-intercalated borophene has also been focused on as a new material due to its high in-plane thermal conductivity²⁶. The single-layer thickness of borophene analogs makes their structure flexible, unlike the structures of other clay minerals or perovskite-type materials, despite being composed of only inorganic components. A dehydration reaction of borophene oxide crystals (BoCs) yields liquid crystals (LCs) (borophene oxide liquid crystals: BoLCs) because of their flexibility, resulting in the development of an inorganic LC device that operates on the basis of dynamic scattering²⁷. Solutions of two-dimensional materials such as antimony phosphate nanosheets²⁸, niobium oxide layered compounds^{29–31}, clay minerals^{32–34}, and graphene or graphene oxides^{35–38} have been reported to show LC phases. In contrast to these lyotropic LCs with organic solvents, BoLCs without solvents have enough and unique possibilities for device applications. The dynamic features of BoLCs are attributable to the potassium cations between layers and the flexible skeleton of the borophene analog, which contributes to generate polarization of charges. In

addition, the BoLC has a substantial advantage in the synthesis of variants because a BoLC with potassium cations (K-BoLC) is prepared by chemical synthesis in a solution phase from potassium borohydride (KBH_4). The metal cations of a BoLC, which directly affect its polarization function, can be simply changed by switching the starting material. In the present study, we synthesized two-dimensional inorganic LC materials, in which alkali cations are alternately stacked in a single layer; we then elucidated the ability of the materials to enhance capacitance between electrodes. The amplification of capacitance by the factor of more than 10^5 achieved by the BoLC samples is not available using existing high-permittivity materials though they have relative dielectric constants of several thousand.

Results

Synthesis of inorganic liquid crystals

At first, BoCs with potassium cations (K-BoC) were synthesized from an acetonitrile solution of KBH_4 according to the method reported in the literature²³. This method, in which the growth of the boron network was controlled by simultaneous crystallization, allows the BoCs to be prepared with other alkali-metal cations (Fig. 1A, B). BoCs with Rb^+ cations (Rb -BoC) or Cs^+ cations (Cs -BoC) were synthesized by the same method using $RbBH_4$ and $CsBH_4$ as raw materials, respectively. In the case of Cs -BoC, crystallization was promoted by using toluene as a poor solvent and concentrating the solution through evaporation. The corresponding LCs (Rb -BoLC and Cs -BoLC) were prepared from the BoCs by heating under vacuum or inert-gas conditions in the same manner as K-BoLC, which proceeded via a dehydration reaction²⁷.

Scanning electron microscopy (SEM) (Fig. 1C) and optical microscopy (Supplementary Fig. 1) images of the synthesized M -BoCs ($M = Rb, Cs$) reveal a flake-like appearance. In the corresponding infrared (IR) spectra, most of the peaks, including the B-O stretching peaks, appear at similar positions (Supplementary Fig. 2). These structures are also confirmed by Raman spectra of M -BoCs ($M = K, Rb, Cs$) complementary (Supplementary Fig. 3). In addition, the B 1s binding energies in M -BoCs ($M = Rb, Cs$) determined by X-ray photo-electron spectroscopy (XPS) are close to that for K-BoC (Supplementary Fig. 4). Collectively, these results suggest that the synthesized M -BoCs ($M = Rb, Cs$) samples have in-plane boron networks similar to that of K-BoC. However, the cations strongly affect the layer spacing of the crystal structure. We characterized the structure of each sample by X-ray diffraction (XRD) analysis (Fig. 2). The observed peaks were fitted with model structures (Supplementary Fig. 5). The initial structure was based on that of K-BoC, whose structure has been determined by

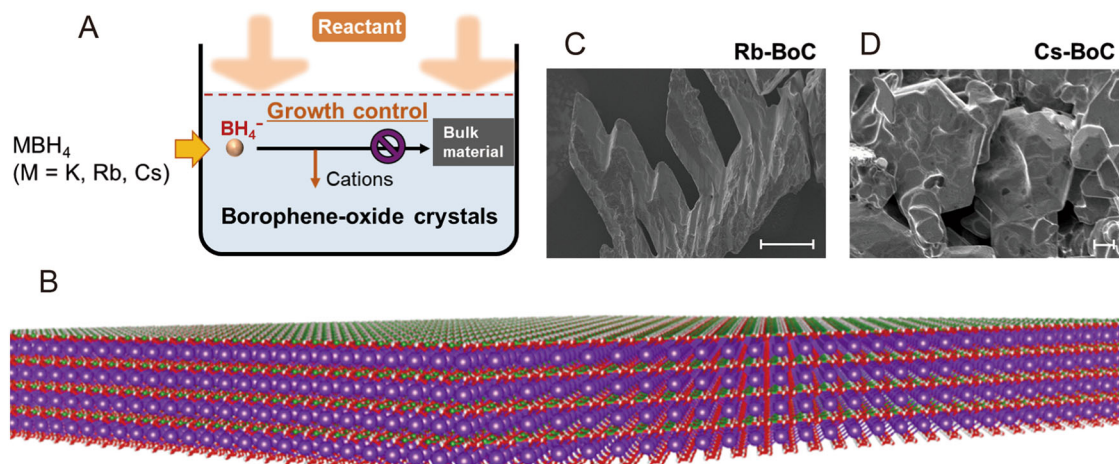


Fig. 1 | Synthesis of borophene oxide layers with metal cations. **A** Schematic of synthesis with structure control. The orange arrows show the reaction of water vapor with MBH_4 ($M = K, Rb, Cs$). **B** Structure of borophene oxide layers (green:

boron, red: oxygen, purple: alkali metal). **C, D** Scanning electron microscopy images of Rb-BoC (scale bar: 100 μ m) and Cs-BoC (scale bar: 10 μ m), respectively.

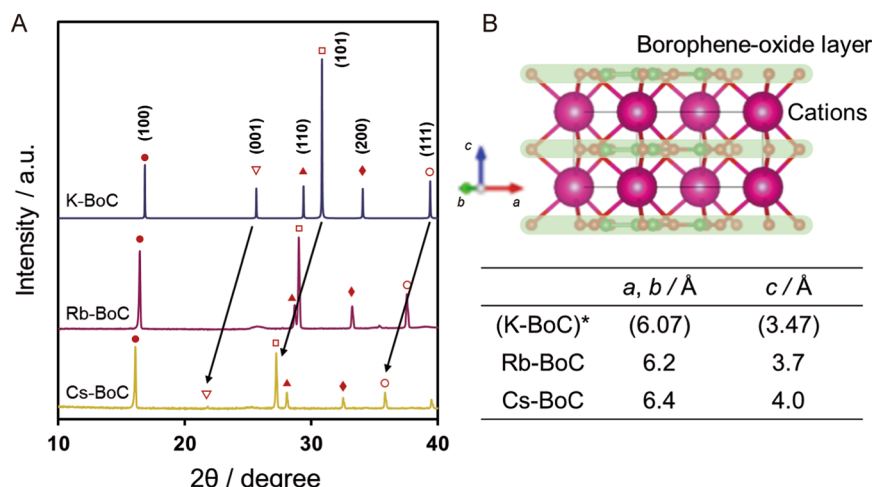


Fig. 2 | Structure analysis of M -BoCs ($M = Rb, Cs$). A XRD spectra of Rb-BoC and Cs-BoC are demonstrated with that of K-BoC. Filled circle: (100), unfilled inverted triangle: (001), filled triangle: (110), unfilled square: (101), filled rhombus: (200),

unfilled circle: (111). **B** Calculated cell lengths ($a = b = 6.2 \text{ \AA}$, and $c = 3.7 \text{ \AA}$ for Rb-BoC, and $a = b = 6.4 \text{ \AA}$, and $c = 4.0 \text{ \AA}$ for Cs-BoC). *Values of single crystal analysis²³.

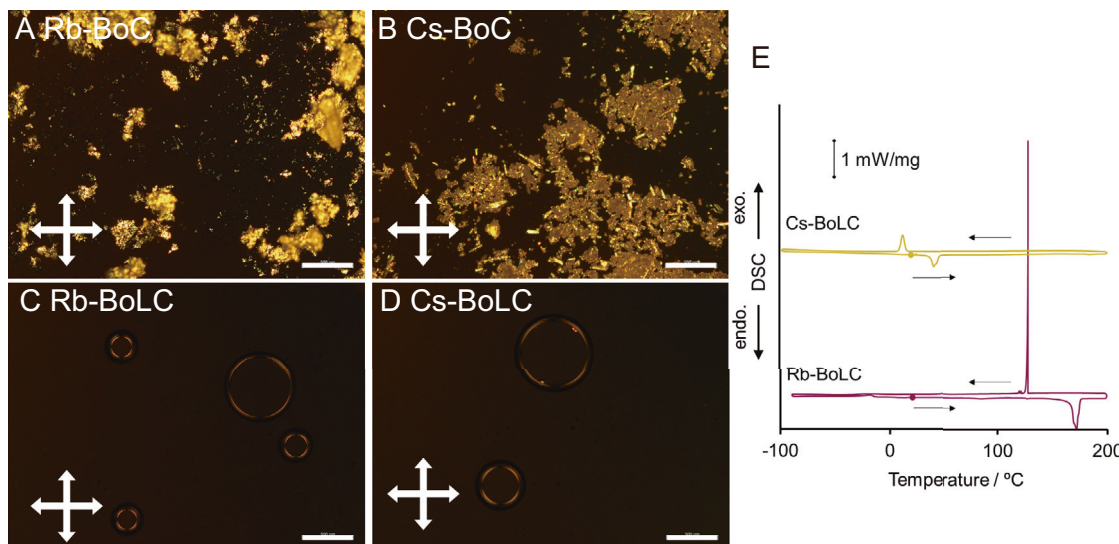


Fig. 3 | Liquid crystalline features of M -BoLCs ($M = Rb, Cs$). A, B Polarized optical microscopy images of M -BoCs ($M = Rb, Cs$) under crossed polarizers (white double arrows). Scale bar: 500 μm . **C, D** Polarized optical microscopy images of M -BoLCs ($M = Rb, Cs$) under crossed polarizers (white double arrows). Scale bar: 500 μm .

E Differential scanning calorimetry (DSC) curves for M -BoLCs ($M = Rb, Cs$) on heating and cooling processes. Filled circles on the curves are starting points of the measurements.

single-crystal structure analysis²³. In the XRD pattern simulated using the corresponding cations and suggested cell parameters obtained from the XRD measurements, almost all the peak positions agree with the observed values. The slight difference in peak intensities is considered to be due to the influence of occupancy of oxygen atoms. The XRD results show that peaks such as (001) and (101), which include c -axis components, are shifted to lower angles in the XRD patterns for M -BoCs ($M = Rb, Cs$) compared with those in the pattern for K-BoC, whereas peaks not related to the c -axis (i.e., 100 and 110) change only slightly. With increasing size of the cations, the 2θ values for the peaks decrease, indicating an increase in the interplanar spacing corresponding to the c -axis direction. Therefore, increasing cation size directly increases the interplanar spacing. The in-plane peak is also shifted, although the change is small; this shift is likely attributable to the cations interacting with oxygen atoms present in the borophene skeleton and the change in size affecting the hexagonal in-plane

structure. As a result, the M -BoCs ($M = Rb, Cs$) were found to have a crystal structure similar to that of K-BoC, with different cell parameters (Rb-BoC: $a = b = 6.2 \text{ \AA}$, $c = 3.7 \text{ \AA}$; Cs-BoC: $a = b = 6.4 \text{ \AA}$, $c = 4.0 \text{ \AA}$) (Fig. 2).

Liquid-crystal features of M -BoLCs ($M = Rb, Cs$)

The M -BoC ($M = Rb, Cs$) samples were subjected to a thermal dehydration reaction, resulting in the formation of LC phase of M -BoLCs ($M = Rb, Cs$) (Fig. 3) after dehydration at 70–150 °C. Decreasing of weight was detected by TG measurements (Supplementary Fig. 6). The details of this change to liquid crystals were already reported in the previous work²⁷. We also confirmed that the in-plane chemical structure was maintained by comparing Raman spectra before and after liquid crystallization (Supplementary Fig. 7). Liquefaction of the multiple crystals and assembly into droplets were observed. Observation of the droplets with a polarized optical microscope under crossed nicols showed four dark areas in the cross direction at the peripheral

region at -200°C , indicating a spherulite-like orientation similar to the case for K-BoLC (Fig. 3C, D). The temperature corresponding to the crystal to LC shift was approximately the same irrespective of the cation species (Supplementary Fig. 6). However, variation of the cations led to a change in the temperature of the phase transition of the BoLCs. K-BoLC has been reported to undergo a thermal phase transition²⁷. Notably, the low-temperature state is totally different from that for BoC because BoLCs are produced by an irreversible dehydration reaction from BoCs; thus, BoLCs are not obtained by the phase transition of BoCs. Thermal analysis of the *M*-BoLCs (*M* = Rb, Cs) reveals that the temperature of the phase transition is lowered to near room temperature as the cation size increases (Fig. 3E), indicating active inorganic LCs over a wider temperature range. This shift of the phase transition temperature to lower values by changing the interlayer cations occurs because the introduction of large Cs^+ , whose surface charge is lower than that of K^+ , weakens the electrostatic interactions between the layers and decreases the crystallinity of the Cs-BoLCs. In the case of Rb-BoLC, a sharp peak was observed in the cooling process. This sharp peak was observed with reproducibility (Supplementary Fig. 8). It is considered that there is a barrier when a large two-dimensional material undergoes a phase transition, resulting in a sudden structural change at a certain temperature. The structures of BoLCs were revealed by powder XRD measurement. In the case of K-BoLC, slight expansion of the distance between layers is reported due to the chemical change in defective B-OH structures via the dehydration process²⁷. In the case of *M*-BoLC (*M* = Rb, Cs), the shift of peaks is not observed compared with the corresponding crystals (Supplementary Fig. 9). The reason is considered to be that, by increasing the size of the cations, the interlayers were already sufficiently expanded, and thus the effect of the chemical reaction at the terminal part was not reflected in the crystal structure.

Capacitance enhancement by BoLCs

The electrostatic capacitance was significantly improved by introducing the BoLCs between the electrodes of a capacitor. Al electrodes were prepared by vapor deposition, with a Cr metal layer for adhesion to the silica substrate (Supplementary Fig. 10). The oxide surface on the Al electrodes was controlled to be 7 nm thick (Fig. 4A). The introduction of K-BoLCs to the electrodes led to a 10^5 -fold increase in capacitance at 200°C compared with that when dry Ar was introduced (Fig. 4B). High dielectric permittivity values of LCs are current hot topics^{39,40}. Though the discussion on the value is difficult due to the effect of interfacial polarizations on the electrode⁴¹, we have estimated that the relative permittivity (ϵ_r) value of K-BoLC was over 10^5 in this device (e.g., 1.2×10^5 at 200°C and 10 at 30°C) through the thickness dependency of the device (Fig. 4C). This value surpasses that of many liquid crystals ($\approx 10^4$) focused on by researchers^{39,40}. The equation is demonstrated in method section. Comparison with the device containing crystal (K-BoC) revealed that the high temperature phase of the K-BoLC is essential for this high dielectric constant in this sample (Supplementary Fig. 11). The capacitance decreased substantially with decreasing temperature (Fig. 4D and Supplementary Fig. 12). As demonstrated in Fig. 4E, the high capacitance was recovered by heating process. This change was found to be reversible, and the on/off ratio exceeded 10^4 times (Fig. 4F and Table 1). The transition temperature was $120\text{--}130^{\circ}\text{C}$ (Fig. 4F), which is similar to the reported phase transition temperature determined from the differential scanning calorimetry (DSC)²⁷. The temperature difference between cooling and heating processes is considered to be derived from supercooling. Stability in multiple charge-discharge processes was also evaluated. At 200°C , the capacitance in a wide frequency region hardly changed during 10 measurements (Fig. 4G, H), confirming enough stability. We note that the stability of a sample decreased at 275°C (Supplementary Fig. 13). The frequency dependence shows a decrease in capacitance in the high-frequency area (Supplementary Fig. 14), suggesting that the

polarization of the sample under the electric field was caused by the migration of ions in a fluid state (Supplementary Fig. 15). Generally, interfacial, dipoles, ionic and electronic contributions are considerable for the increase of the polarization⁴². In the case of K-BoLC, a large decrease was observed when the frequency exceeded about 10^3Hz . Therefore, major influence of the interfacial polarization is considered. This feature suggests that the cations are unbound and movable in the K-BoLC layers. The cations can move on with low frequency; on the other hand, the cations cannot move on with high frequency. Therefore, it is suggested that this motion of cations enhances the capacitance of the K-BoLC in low frequency region. In this frequency region, the loss tangent is restricted. In high frequency, the values of loss tangent, which is an index of energy loss, increased according to the frequency (Supplementary Fig. 16), because the cations of K-BoLC do not perfectly but halfway follow the frequency.

Discussions

The formation of the K-BoLCs between the plates was proved by temperature-dependent XRD analysis. Two sapphire substrates were used for sandwiching K-BoLC because of the silent background peaks of sapphire. As a result, the diffraction peaks disappeared except for one broad peak originating from the ordered structures under the high-temperature condition associated with high capacitance (Supplementary Figs. 17 and 18). Since multiple peaks were observed upon returning to room temperature, the structural change is reversible, similar to the change in dielectric constant (Supplementary Fig. 17). The results suggest that the cations and the two-dimensional boron sheets maintain the layered structures even at high temperatures. In this device, a homogeneous alignment of BoLCs to the electrodes was not observed. Polarized optical microscopy images suggested that the BoLCs between glass plates (thickness: 0.1–0.2 mm) formed poly-domain structures (Supplementary Fig. 19), implying that those oriented perpendicular to the electrodes affect the interfacial polarization.

The capacitance change behavior was also observed in the case of the other investigated cations. The capacitances of *M*-BoLCs (*M* = Rb, Cs) measured at 200°C show similar values for K-BoLC (Fig. 5A). Also, the temperature at which the capacitance changes is about 100°C for both Rb-BoLC and Cs-BoLC; the temperatures are lower than the corresponding temperature for K-BoLC. The trend in temperature shift is consistent with the phase transition temperatures of the LCs. The introduced cations also strongly affected the frequency dependence (Fig. 5B). The retention of high capacitance in the high-frequency region was observed in the case of larger cations. This is attributed to increased distances between layers for the larger cations, which allows ions with weak ionic bindings to move in a wide space. Since theoretical calculations are a powerful method to clarify the effects of cations, we demonstrated the movement of potassium ions in K-BoC based on molecular dynamics calculations using a model with partial potassium deficiency (Supplementary Movie 1). This result suggested that the distance of 1.13 nm between layers is required in order for potassium cations to move in the plane at 500K (202°C). First-principles calculations to investigate the interlayer distance dependency in K-BoC revealed that it takes multiple minimum structures with the change of the magnetic moment (Supplementary Fig. 20). We are considering that this structural feature may assist the partial opening between layers for the movement of potassium cations. However, detailed discussion is difficult at present because positions of oxygens are still ambiguous in BoC and BoLC.

In conclusion, a synthesis strategy for ion-laminated boron layered materials in a solution phase was demonstrated, allowing the generation of analogs by varying the alkali-metal species. The incorporation of large cations expanded the thermal stability range of LC phases due to weakened ionic interactions between borophene-like layers. Evaluating the capacitance of ion-laminated structures revealed

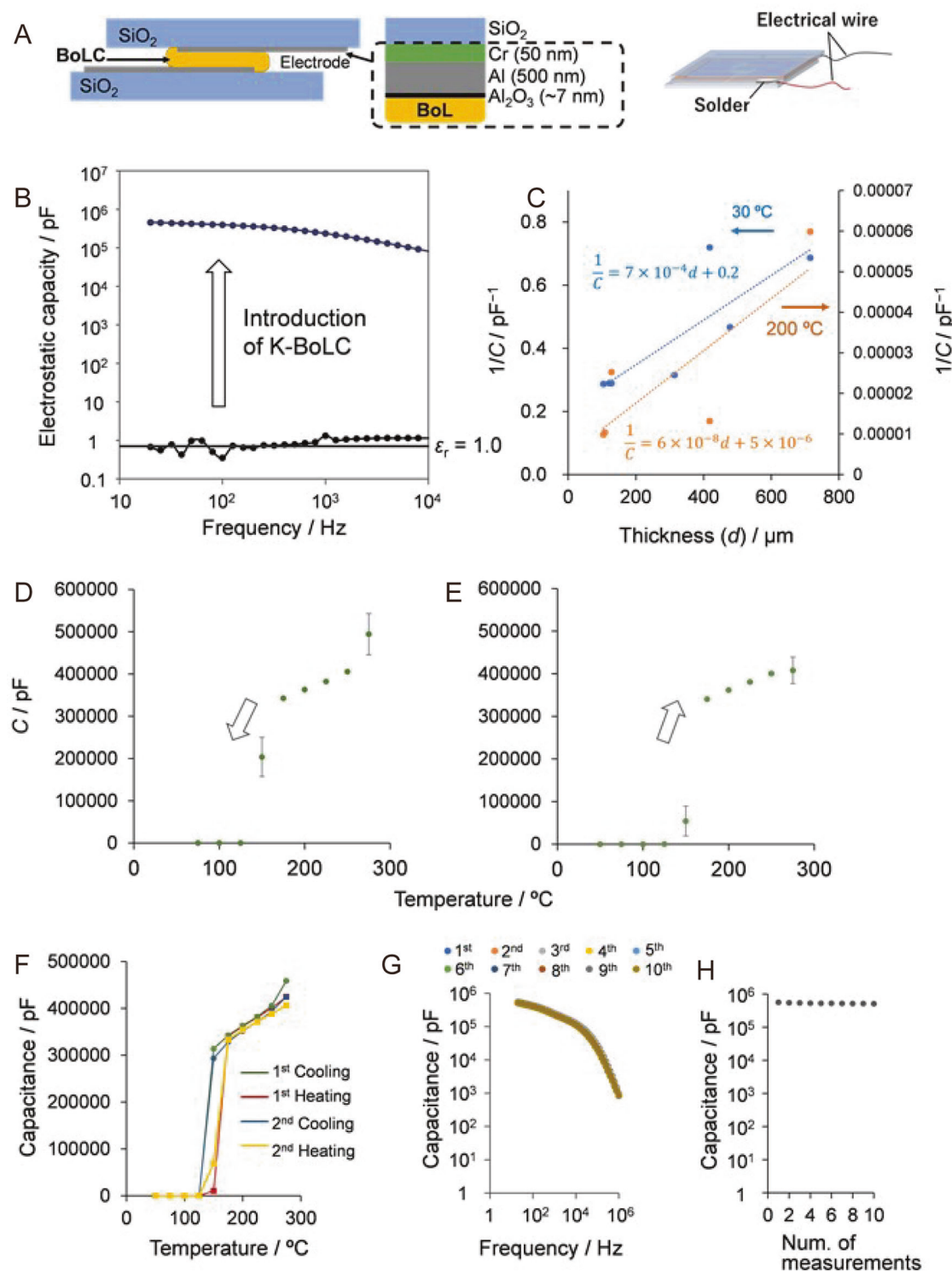


Fig. 4 | Electrostatic capacity enhancement by K-BoLCs. **A** Set-up of the capacitance measurement device for BoLCs. Details are described in Supplementary Materials. **B** Change of the electrostatic capacity by introducing K-BoLC between electrodes with 0.13 mm distance. The applied voltage and temperature are 100 mV and 275 °C, respectively. **C** Thickness dependency of the capacitance device at 200 and 30 °C. Temperature dependency of the electrostatic capacity of the K-BoLC device during cooling (**D**) or heating (**E**) processes. The transition temperature is

corresponding to the phase transition of K-BoLC. Error bars in (**D**) and (**E**) stand for the standard deviation of four or five observed values. These data were obtained using a separately prepared device. **F** Reversibility of the electrostatic capacity of the K-BoLC device against temperature changes. **G**, **H** Stability of the device during multiple measurements. Frequency dependence (**G**) and capacitance decay (**H**) are demonstrated.

a 10⁵-fold or greater increase when borophene-like materials were introduced between electrodes. This achievement significantly contributes to the advancement of novel device applications for borophene analogs, which are anticipated as post-graphene materials.

Methods

Fabrication of *M*-BoC (*M* = K, Rb, Cs)

MBH_4 ($M = \text{K}$: 125 mg, $M = \text{Rb}$: 80 mg, $M = \text{Cs}$: 137 mg) was added to acetonitrile ($M = \text{K}$: 500 mL, $M = \text{Rb}$ or Cs : 200 mL) in an Ar-filled glove

box. The mixture was stirred for 1 h. The solution was then heated in air at 40 °C for 1 h and left to stand for 20 h. Afterward, the solution was filtered to remove any undissolved solids. The filtered solution was then placed in a vial with the lid slightly open and left undisturbed for several days until crystals formed. In the case of Cs-BoC, crystallization was promoted by using toluene as a poor solvent and concentrating the solution through evaporation.

Preparation of *M*-BoLC (*M* = K, Rb, Cs)

Crushed *M*-BoC (*M* = K, Rb, Cs) was sandwiched between substrates and heated at 200 °C for 2 h under vacuum.

Characterization

Field-emission SEM observations were carried out with a Hitachi High-Technologies S5500. Polarized optical microscopy images were acquired using an Olympus BX50 or BX53-P, or a Nikon Eclipse E400 POL with halogen lamps; the temperature of the specimens was controlled using a Mettler Toledo FP-90 or FP-82HT or an Instec HCS402.

The samples shown in Fig. 3A–D were prepared using glass cells and polyimide film (Kapton) as a spacer. The sides of the cells were fastened with Araldite bond (Araldite RT30). DSC curves were recorded using a Rigaku DSC 8230 or a Hitachi High-Technologies DSC 7000X. The DSC curves in Fig. 3E were recorded after thermal treatment of Rb-BoC (4.7 mg) and Cs-BoC (3.3 mg) in an Al sample pan under a N₂ atmosphere. FT-IR spectra were acquired using a Jasco FT/IR-4700; samples were prepared as KBr pellets. XRD data were collected using a Rigaku SmartLab. Raman spectra were recorded using a confocal microscope laser Raman spectrometer (Horiba LabRAM HR Evolution) with the excitation wavelength set to 632.8 nm from a He-Ne laser with a typical power of 0.5 mW on the sample surface. Samples for Fig. S7 were placed in a glass capillary for measurement to avoid decomposition due to air exposure. Glass capillaries were heated at 200 °C for 5 min allowing to transform to LCs. XPS spectra were measured by using an ESCA-3400 (Shimadzu) or a PHI 5000 VersaProbe (Ulvac-Phi, Inc.) equipped with an Al K α (15 kV, 25 W). The measured samples on a carbon tape were crushed by a spatula to bare flesh

surfaces before measurements. Obtained data were analyzed with the PHI Multipack software.

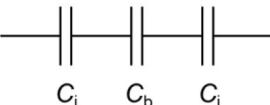
TG-DTA and DSC curves were recorded by using a Rigaku TG 8120, and a DSC 7000X (Hitachi High-Tech Science Corporation), respectively. Mettler thermo system: METTLER TOLEDO FP90 Hot Stage (METTLER TOLEDO) and LCR meter: Precision LCR meter, 4284 A, 20 Hz–1 MHz (Agilent) was used for capacitance measurements.

Capacitance measurements

Crashed BoCs were evenly placed on the aluminum electrode. Kapton films were also put next to the sample as a space to control the distance (0.1–0.2 mm) between the electrodes as need. Then it was sandwiched with another electrode, and three sides of the both electrodes were sealed with an epoxy-based adhesive (Araldite Rapid). After fixed, it was heated to 200 °C under vacuum to prepare BoLCs. After cooling to room temperature, the remaining one side was sealed with Araldite Rapid under an inert gas condition. Electric wires are attached to the aluminum electrodes with ultrasonic soldering for capacitance measurements. The thickness of the device was changed by varying the amount of BoC samples before thermal treatment to produce BoLCs.

The relative permittivity (ϵ_r) is evaluated from the Eq. (1) and Fig. 4C. C_b : capacitance of sample, C_i : interfacial capacitance, ϵ_r : vacuum permittivity, S : surface area of the electrode, d : distance of sample:

$$\begin{aligned}
 \frac{1}{C} &= \frac{1}{C_i} + \frac{1}{C_b} + \frac{1}{C_i} \\
 &= \frac{2}{C_i} + \frac{1}{C_b} \\
 &= \frac{2}{C_i} + \frac{1}{\epsilon_0 \epsilon_r S} d
 \end{aligned} \tag{1}$$



A capacitance measurement device of BoC was prepared with the thickness of 0.1–0.2 mm. After sealing the sides of the device, capacitance measurements were subjected without heating treatment at 200 °C.

Calculation

The Vienna ab initio simulation package (VASP)^{43–46} was used to evaluate the thermal stability of the structure of the modeled borophene oxide layer in the framework of density functional theory (DFT). We used the generalized gradient approximation of Perdew, Burke, and Ernzerhof⁴⁷ as the exchange-correlation potential. The projector augmented wave method^{48,49} was used to solve the Korn-Sham equation. The cut-off energy is set to 500 eV. Thus, we did not apply it in this

Table 1 | The electrostatic capacity values of the K-BoLC device during cooling or heating processes

Temperature/°C	C/pF	
	Cooling	Heating
275	$(4.9 \pm 0.5) \times 10^5$	$(4.1 \pm 0.3) \times 10^5$
150	$(2.0 \pm 0.5) \times 10^5$	$(5.4 \pm 3.5) \times 10^4$
100	42 ± 34	12 ± 4

The error values stand for the standard deviation of four or five observed values.

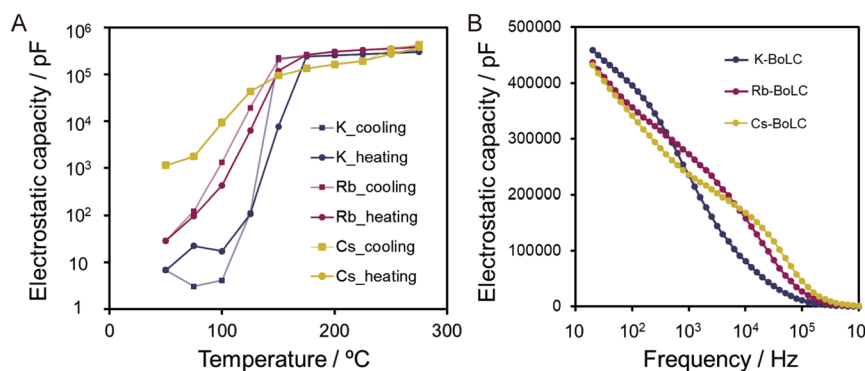


Fig. 5 | Electrostatic capacity measurement of *M*-BoLCs (*M* = K, Rb, and Cs). Temperature (A) or frequency (B) dependencies of the electrostatic capacities for *M*-BoLCs (*M* = K, Rb, Cs). The frequency of (A) is 20 Hz, and the temperature of (B) is 275 °C.

study to save computational cost. VESTA⁵⁰ was used for drawing the structures and simulating the scattering patterns.

VASP version 5.4.1 was used for the simulation. GGA-PBE was used for exchange-correlation functionals, and PAW method was used for pseudopotentials. In order to investigate the effect of interlayer distance, one-point calculations were performed while changing interlayer distance in 5% increments based on the experimentally observed value, preserving the relative atomic coordinates within the cell (Supplementary Fig. 20). The molecular dynamics simulations were in the NVT ensemble with a time step of 1 fs. The in-plane structure of the calculated system is prepared after optimization from the experimental data. To reveal the transition of potassium cations, one defect was introduced with a fixed boron network.

Reporting summary

Further information on research design is available in the Nature Portfolio Reporting Summary linked to this article.

Data availability

All data in the main text or the Supplementary Materials are available upon request.

References

1. Cohen, R. E. Origin of ferroelectricity in perovskite oxides. *Nature* **358**, 136–138 (1992).
2. Bhalla, A. S., Guo, R. & Roy, R. The perovskite structure—a review of its role in ceramic science and technology. *Mater. Res. Innov.* **4**, 3–26 (2000).
3. Akishige, Y., Oomi, G., Yamaoto, T. & Sawaguchi, E. Dielectric properties of ferroelectric hexagonal BaTiO₃. *J. Phys. Soc. Jpn.* **58**, 930–939 (1989).
4. Li, B.-W. et al. Atomic layer engineering of high- κ ferroelectricity in 2D perovskites. *J. Am. Chem. Soc.* **139**, 10868–10874 (2017).
5. Matte, H. S. S. R. et al. MoS₂ and WS₂ analogues of graphene. *Angew. Chem. Int. Ed.* **49**, 4059–4062 (2010).
6. Coleman, J. N. et al. Two-dimensional nanosheets produced by liquid exfoliation of layered materials. *Science* **331**, 568–571 (2011).
7. Vogt, P. et al. Silicene: compelling experimental evidence for graphenelike two-dimensional silicon. *Phys. Rev. Lett.* **108**, 155501 (2012).
8. Feng, B. et al. Evidence of silicene in honeycomb structures of silicon on Ag(111). *Nano Lett.* **12**, 3507–3511 (2012).
9. Mannix, A. J. et al. Synthesis of borophenes: anisotropic, two-dimensional boron polymorphs. *Science* **350**, 1513–1516 (2015).
10. Feng, B. et al. Experimental realization of two-dimensional boron sheets. *Nat. Chem.* **8**, 563–568 (2016).
11. Dávila, M. E., Xian, L., Cahangirov, S., Rubio, A. & Lay, G. L. Germanene: a novel two-dimensional germanium allotrope akin to graphene and silicene. *N. J. Phys.* **16**, 095002 (2014).
12. Ji, J. et al. Two-dimensional antimonene single crystals grown by van der Waals epitaxy. *Nat. Commun.* **7**, 13352 (2016).
13. Zhu, F.-F. et al. Epitaxial growth of two-dimensional stanine. *Nat. Mater.* **14**, 1020–1025 (2015).
14. Reis, F. et al. Bismuthene on a SiC substrate: a candidate for a high-temperature quantum spin Hall material. *Science* **357**, 287–290 (2017).
15. Zhu, Z. et al. Multivalency-driven formation of Te-based monolayer materials: a combined first-principles and experimental study. *Phys. Rev. Lett.* **119**, 106101 (2017).
16. Mannix, A. J., Zhang, Z., Guisinger, N. P., Yakobson, B. I. & Hersam, M. C. Borophene as a prototype for synthetic 2D materials development. *Nat. Nanotechnol.* **13**, 444–450 (2018).
17. Chen, C. et al. Synthesis of bilayer borophene. *Nat. Chem.* **14**, 25–31 (2022).
18. Ebrahimi, M. The birth of bilayer borophene. *Nat. Chem.* **14**, 3 (2022).
19. Liu, X. et al. Borophene synthesis beyond the single-atomic-layer limit. *Nat. Mater.* **21**, 35–40 (2022).
20. Li, Q. et al. Synthesis of borophane polymorphs through hydrogenation of borophene. *Science* **371**, 1143–1148 (2021).
21. Kambe, T. et al. π -conjugated nickel bis(dithiolene) complex nanosheet. *J. Am. Chem. Soc.* **135**, 2462–2465 (2013).
22. Kambe, T. et al. Redox control and high conductivity of nickel bis(dithiolene) complex π -nanosheet: a potential organic two-dimensional topological insulator. *J. Am. Chem. Soc.* **136**, 14357–14360 (2014).
23. Kambe, T., Hosono, R., Imaoka, S., Kuzume, A. & Yamamoto, K. Solution phase mass synthesis of 2D atomic layer with hexagonal boron network. *J. Am. Chem. Soc.* **141**, 12984–12988 (2019).
24. Kambe, T., Nishihara, H. & Yamamoto, K. Chemical bottom-up approach for inorganic single-atomic layers aiming beyond graphene. *Dalton Trans.* **52**, 15297–15302 (2023).
25. Nishino, H. et al. Formation and characterization of hydrogen boride sheets derived from MgB₂ by cation exchange. *J. Am. Chem. Soc.* **139**, 13761–13769 (2017).
26. Hu, Y. et al. Three-fold enhancement of in-plane thermal conductivity of borophene through metallic atom intercalation. *Nano Lett.* **20**, 7619–7626 (2020).
27. Kambe, T. et al. Liquid crystalline 2D borophene oxide for inorganic optical devices. *Nat. Commun.* **13**, 1037 (2022).
28. Gabriel, J.-C. P. et al. Swollen liquid-crystalline lamellar phase based on extended solid-like sheets. *Nature* **413**, 504–508 (2001).
29. Miyamoto, N. & Nakato, T. Liquid crystalline nature of K₄Nb₆O₁₇ nanosheet sols and their macroscopic alignment. *Adv. Mater.* **14**, 1267–1270 (2002).
30. Nakato, T., Miyamoto, N. & Harada, A. Stable liquid crystalline phases of colloidally dispersed exfoliated layered niobates. *Chem. Commun.* 78–79 <https://doi.org/10.1039/B309628A> (2004).
31. Miyamoto, N., Yamamoto, S., Shimasaki, K., Harada, K. & Yamauchi, Y. Exfoliated nanosheets of layered perovskite KCa₂Nb₃O₁₀ as an inorganic liquid crystal. *Chem. Asian J.* **6**, 2936–2939 (2011).
32. Michot, L. J. et al. Liquid-crystalline aqueous clay suspensions. *PNAS* **103**, 16101–16104 (2006).
33. Michot, L. J. et al. Sol/gel and isotropic/nematic transitions in aqueous suspensions of natural nontronite clay. influence of particle anisotropy. 1. Features of the I/N transition. *Langmuir* **24**, 3127–3139 (2008).
34. Michot, L. J. et al. Sol-gel and isotropic/nematic transitions in aqueous suspensions of natural nontronite clay. Influence of particle anisotropy. 2. Gel structure and mechanical properties. *Langmuir* **25**, 127–139 (2009).
35. Aboutalebi, S. H., Gudarzi, M. M., Zheng, Q. B. & Kim, J.-K. Spontaneous formation of liquid crystals in ultralarge graphene oxide dispersions. *Adv. Funct. Mater.* **21**, 2978–2988 (2011).
36. Kim, J. E. et al. Graphene oxide liquid crystals. *Angew. Chem. Int. Ed.* **50**, 3043–3047 (2011).
37. Xu, Z. & Gao, C. Aqueous liquid crystals of graphene oxide. *ACS Nano* **5**, 2908–2915 (2011).
38. Xu, Z. & Gao, C. Graphene chiral liquid crystals and macroscopic assembled fibres. *Nat. Commun.* **2**, 571 (2011).
39. Nishikawa, H. et al. A fluid liquid-crystal material with highly polar order. *Adv. Mater.* **29**, 1702354 (2017).
40. Li, J. et al. Development of ferroelectric nematic fluids with giant- ϵ dielectricity and nonlinear optical properties. *Sci. Adv.* **7**, eabf5047 (2021).
41. Erkoreka, A., Martínez-Perdiguero, J., Mandle, R. J., Mertelj, A. & Sebastián, N. Dielectric spectroscopy of a ferroelectric nematic liquid crystal and the effect of the sample thickness. *J. Mol. Liq.* **387**, 122566 (2023).

42. Liu, S., Shen, B., Haoa, H. & Zhai, J. Glass-ceramic dielectric materials with high energy density and ultra-fast discharge speed for high power energy storage applications. *J. Mater. Chem. C* **7**, 15118 (2019).
43. Kresse, G. & Furthmüller, J. Efficient iterative schemes for ab initio total-energy calculations using a plane-wave basis set. *Phys. Rev. B Condens. Matter Mater. Phys.* **54**, 11169–11186 (1996).
44. Kresse, G. & Hafner, J. Ab initio molecular dynamics for liquid metals. *Phys. Rev. B* **47**, 558–561 (1993).
45. Kresse, G. & Hafner, J. Ab initio molecular-dynamics simulation of the liquid-metal-amorphous-semiconductor transition in germanium. *Phys. Rev. B* **49**, 14251–14269 (1994).
46. Kresse, G. & Furthmüller, J. Generalized gradient approximation made simple. *Comput. Mater. Sci.* **6**, 15–50 (1996).
47. Perdew, J. P., Burke, K. & Ernzerhof, M. Generalized gradient approximation made simple. *Phys. Rev. Lett.* **77**, 3865–3868 (1996).
48. Blöchl, P. E. Projector augmented-wave method. *Phys. Rev. B* **50**, 17953–17979 (1994).
49. Kresse, G. & Joubert, D. From ultrasoft pseudopotentials to the projector augmented-wave method. *Phys. Rev. B Condens. Matter Mater. Phys.* **59**, 1758–1775 (1999).
50. Momma, K. & Izumi, F. VESTA 3 for three-dimensional visualization of crystal, volumetric and morphology data. *J. Appl. Crystallogr.* **44**, 1272–1276 (2011).

Acknowledgements

The authors are grateful to Material Analysis Division (Suzukakedai), Open Facility Center, Tokyo Institute of Technology for XRD and XPS analysis, BLO2B1 of SPring-8 with the approval of the Japan Synchrotron Radiation Research Institute (JASRI) (Proposal No. 2023A1708) and Advanced Research Infrastructure for Materials and Nanotechnology in Japan (ARIM) of the Ministry of Education, Culture, Sports, Science and Technology (MEXT), Grant Number JPMXP1223UT0034 (K. Okitsu, K. Fukawa, K. Isagai). The computational analysis was partly carried out using the TSUBAME4.0 supercomputer at Institute of Science Tokyo. This work was partly supported by Fusion Oriented Research for disruptive Science and Technology grant Number JPMJFR2231 (T.K.), Japan Society for the Promotion of Science (23H02043 (T.K.), 22H04507 (T.K.), 21K05125 (A.K.)), Exploratory Research for Advanced Technology grant Number JPMJER1503 (K.Y.), The Ogasawara Memorial Foundation (T.K., A.K.), and The Sumitomo Foundation (A.K.). This work was performed under the Cooperative Research Program of “Network Joint Research Center for Materials and Devices”. This work was performed under the Research Program of “Dynamic Alliance for Open Innovation Bridging Human, Environment and Materials” and “Crossover Alliance to Create the Future with People, Intelligence and Materials” in “Network Joint Research Center for Materials and Devices”.

Author contributions

T.K., M.K., H.T., T.Y., H.N., M.Y., A.K., K.A., R.I., J.K., S.M., S.K., H.I., and A.S. carried out experiments. Calculations were conducted by M.Y. through discussion with T.K. T.K., H.I., A.S., and K.Y. contributed to design of the research. T.K., M.K., H.T., and M.Y. wrote the manuscript through discussion with S.M., H.I., A.S., and K.Y. All authors have given approval to the final version of the manuscript.

Competing interests

The authors declare no competing interests.

Additional information

Supplementary information The online version contains supplementary material available at <https://doi.org/10.1038/s41467-024-55307-6>.

Correspondence and requests for materials should be addressed to Tetsuya Kambe or Kimihisa Yamamoto.

Peer review information *Nature Communications* thanks Gang Zhang, who co-reviewed with Shuai Chen, Kehui Wu and the other, anonymous, reviewer(s) for their contribution to the peer review of this work. A peer review file is available.

Reprints and permissions information is available at <http://www.nature.com/reprints>

Publisher's note Springer Nature remains neutral with regard to jurisdictional claims in published maps and institutional affiliations.

Open Access This article is licensed under a Creative Commons Attribution-NonCommercial-NoDerivatives 4.0 International License, which permits any non-commercial use, sharing, distribution and reproduction in any medium or format, as long as you give appropriate credit to the original author(s) and the source, provide a link to the Creative Commons licence, and indicate if you modified the licensed material. You do not have permission under this licence to share adapted material derived from this article or parts of it. The images or other third party material in this article are included in the article's Creative Commons licence, unless indicated otherwise in a credit line to the material. If material is not included in the article's Creative Commons licence and your intended use is not permitted by statutory regulation or exceeds the permitted use, you will need to obtain permission directly from the copyright holder. To view a copy of this licence, visit <http://creativecommons.org/licenses/by-nc-nd/4.0/>.

© The Author(s) 2025